Results in Engineering 32 (2026) 112560

Contents lists available at ScienceDirect

Results in Engineering

journal homepage: www.sciencedirect.com/journal/results-in-engineering

Research paper

# $Sb_2Se_3/MAPbI_3$ thin-film solar cells: Interface engineering and performance enhancement

Danial Keighobadi [a], Ali Asghar Orouji [a], Mehdi Mousavi-Kamazani [b], Mohammad Danaie [a,*]

[a] Faculty of Electrical and Computer Engineering, Semnan University, Semnan, Iran
[b] Department of Nanotechnology, Faculty of New Sciences and Technologies, Semnan University, Semnan, Iran

ARTICLE INFO

*Keywords:*
$Sb_2Se_3$thin-film solar cell
$MAPbI_3$
Dual-absorber heterojunction
$TiO_2$ interlayer
Interface engineering
SCAPS-1D

ABSTRACT

A dual-absorber thin-film solar cell architecture based on $Sb_2Se_3/MAPbI_3/TiO_2/ZnO/Al:ZnO$ is designed and numerically optimized using the SCAPS-1D simulator. The distinguishing feature of this work is the experimentally calibrated redesign of a conventional $Sb_2Se_3/CdS$ device, in which $Sb_2Se_3$ is retained as the primary absorber, a thin $MAPbI_3$ layer is introduced as a secondary absorber and heterojunction-forming layer, and $TiO_2$ is specifically employed to engineer the $MAPbI_3/ZnO$ interface. The environmentally friendly $Sb_2Se_3$ serves as the primary absorber, while $MAPbI_3$ functions as the secondary absorber, forming a heterojunction that promotes efficient charge separation and suppresses interface recombination. The inclusion of a $TiO_2$ buffer layer between $MAPbI_3$ and ZnO effectively aligns the energy bands and reduces carrier leakage losses. Comparative analysis with the conventional $Sb_2Se_3/CdS/ZnO$ reference structure demonstrates that replacing the *CdS* buffer with $MAPbI_3$, together with the incorporation of a $TiO_2$ interlayer, increases the power conversion efficiency from approximately 10.12% to 18.44%, accompanied by notable improvements in $J_{sc}$, $V_{oc}$, and fill factor (FF). The optimized configuration achieves a power conversion efficiency of 18.44%, with Jsc = 34.05 mA·cm$^{-2}$, $V_{oc}$ = 0.77 V, and FF = 70.34%, representing a substantial improvement over the reference device (PCE =10.12%). Simulation-based impedance spectroscopy and capacitance–frequency analyses indicated improved interfacial charge-transport characteristics, reduced capacitive dispersion, and more stable carrier response in the proposed device. Furthermore, the optimal $Sb_2Se_3$ absorber thickness of 2.6 μm was determined, balancing enhanced optical absorption with limited bulk recombination losses. Overall, the results demonstrate that substituting CdS with $MAPbI_3$ and incorporating $TiO_2$ as an energy buffer provides an effective route for enhancing the photovoltaic performance, interface stability, and environmental compatibility of $Sb_2Se_3$-based thin-film solar cells. This approach provides a promising route toward high-efficiency, Cd-free, and potentially cost-effective dual-absorber photovoltaic devices, although further development of Pb-free alternatives is required for fully environmentally benign implementation.

## 1. Introduction

Thin-film solar cells have emerged in recent years as one of the most promising candidates for next-generation photovoltaic technologies, primarily due to advantages such as low fabrication cost, compatibility with low-temperature processing, lightweight structure, and their ability to be integrated onto flexible substrates [1–3]. Nevertheless, achieving higher power-conversion efficiencies requires overcoming several fundamental challenges, including interfacial recombination, improper band alignment between adjacent layers, and inefficient carrier extraction. Addressing these issues demands systematic materials engineering and careful optimization of the device architecture [4–8].

Among thin-film absorbers, $Sb_2Se_3$ has attracted considerable attention owing to its environmentally benign and earth-abundant constituents, a suitable bandgap typically reported in the range of approximately 1.1–1.2 eV, adequate carrier diffusion length, and high absorption coefficient exceeding [7–10].

The environmentally benign nature of $Sb_2Se_3$ is primarily attributed to the absence of highly toxic cadmium and the earth-abundant nature of its constituent elements. Compared with conventional Cd-based

* Corresponding author.
*E-mail address:* danaie@semnan.ac.ir (M. Danaie).

https://doi.org/10.1016/j.rineng.2026.112560
Received 30 June 2026; Received in revised form 9 August 2026; Accepted 19 August 2026
Available online 23 August 2026

compounds such as CdS or CdTe, $Sb_2Se_3$ offers a more sustainable absorber platform and avoids the environmental and health concerns associated with cadmium processing and disposal. In addition, $Sb_2Se_3$ does not rely on scarce or critical elements such as indium or gallium, further improving its long-term sustainability. However, in the present device, the incorporation of $MAPbI_3$ introduces lead (Pb), which is a toxic heavy metal. Therefore, the proposed architecture cannot be considered fully non-toxic, but rather a partially improved alternative in which Cd-based materials are replaced. Recent studies have demonstrated the development of truly environmentally friendly $Sb_2Se_3$-based solar cells using Pb-free and Cd-free configurations [11–13], highlighting the importance of further material innovation toward fully sustainable photovoltaic technologies.

The commonly used reference configuration is $Sb_2Se_3$/CdS/ZnO/Al:ZnO [14]. Although CdS functions as a conventional and moderately effective n-type buffer layer, its parasitic absorption in the blue region of the spectrum, the formation of interfacial traps at the CdS/$Sb_2Se_3$ interface, and its environmental concerns restrict the efficiency of this structure to approximately 10.12%. In addition to band-alignment and interface engineering, various optical light-trapping strategies have been widely explored to enhance photon harvesting in thin-film solar cells, including $Sb_2Se_3$-based devices. These approaches include surface texturing to increase the effective optical path length, incorporation of metallic nanoparticles to induce surface plasmon resonance (SPR), and the use of diffractive or photonic structures to improve light coupling and absorption. While such strategies can significantly enhance photocurrent generation, their effectiveness often comes at the expense of increased fabrication complexity and process sensitivity. In this context, electrical optimization through interface and band-alignment engineering, as pursued in the present work, represents a complementary pathway for improving device performance without introducing additional optical complexity.

Considering the intrinsic drawbacks of CdS, recent studies have increasingly focused on alternative n-type absorbers or buffer layers with larger bandgaps and better carrier extraction characteristics [15–17]. One of the most promising strategies is the incorporation of a secondary absorber with a higher bandgap [18–21]. Such a layer not only enhances the absorption of high-energy photons but also improves band alignment and suppresses interface recombination, thereby promoting more efficient charge separation and transport [22–24].

Previous studies suggest that the $Sb_2Se_3$/$MAPbI_3$ heterojunction may provide a favorable energy-level arrangement for spatial carrier separation. This possibility motivates the investigation of $MAPbI_3$ as a secondary absorber in the present architecture. However, the actual band alignment and carrier-transport behavior depend on the adopted material and interface parameters and are therefore evaluated numerically only after calibration of the reference model.

The hybrid organic–inorganic perovskite $MAPbI_3$ has been widely investigated in various hybrid and tandem photovoltaics due to its 1.55 eV bandgap, exceptionally high absorption coefficients, favorable carrier transport properties, and tunable energy levels [25–30]. Although $MAPbI_3$ suffers from stability challenges when used as a standalone primary absorber, its integration as a secondary, high-bandgap layer alongside a chemically robust and stable material such as $Sb_2Se_3$ can substantially enhance current generation and create a more favorable band-alignment landscape [31–36].

Several studies examining $Sb_2Se_3$/$MAPbI_3$ hybrid structures have demonstrated that these two materials exhibit chemical, phase, and electronic compatibility, with a low tendency to form undesirable secondary phases at their interface [26]. Moreover, a band alignment has been reported for this heterojunction, enabling efficient spatial separation of charge carriers. These findings provide a solid foundation for incorporating into our design, even though the reference structure in this work is based on CdS [37–41].

Previous SCAPS-1D studies on $Sb_2Se_3$-based solar cells have mainly focused on band-alignment optimization, replacement of CdS with alternative buffer layers, incorporation of carrier-selective layers, and optimization of absorber thickness, doping concentration, and defect properties [18–20,25]. Related SCAPS-based studies have also investigated multilayer and heterojunction photovoltaic architectures incorporating alternative chalcogenide or perovskite absorbers [28,40,41]. In addition, the experimental compatibility of $Sb_2Se_3$ and $MAPbI_3$ has previously been demonstrated in a perovskite-centered device in which $Sb_2Se_3$ primarily served as a hole-transport material [26]. Against this background, the present work is distinguished by the controlled redesign of an experimentally reported $Sb_2Se_3$/CdS/ZnO/Al:ZnO reference device. In the proposed architecture, $Sb_2Se_3$ remains the primary absorber, a thin $MAPbI_3$ layer functions as a secondary absorber and heterojunction-forming layer, and $TiO_2$ is deliberately inserted between $MAPbI_3$ and ZnO to engineer the conduction-band offset and electron selectivity. Therefore, the contribution of this study lies in the experimentally calibrated, $Sb_2Se_3$-centered integration and separate evaluation of CdS replacement, dual-absorber coupling, and $MAPbI_3$/$TiO_2$/ZnO interface engineering, rather than in the individual use of these constituent materials.

In this study, an experimentally anchored $Sb_2Se_3$-centered dual-absorber architecture consisting of $Sb_2Se_3$/$MAPbI_3$/$TiO_2$/ZnO/Al:ZnO was numerically investigated. The device was developed through a controlled modification of the experimentally validated $Sb_2Se_3$/CdS/ZnO/Al:ZnO reference structure rather than through the independent assembly of an idealized multilayer stack. In the proposed configuration, $Sb_2Se_3$ remains the primary low-bandgap absorber, whereas the thin $MAPbI_3$ layer acts as a secondary absorber and forms a type-II heterojunction with $Sb_2Se_3$. The $TiO_2$ interlayer is specifically introduced between $MAPbI_3$ and ZnO to control the conduction-band offset, improve electron selectivity, suppress hole leakage, and reduce interfacial charge accumulation. ZnO and Al:ZnO subsequently provide electron transport and transparent current collection, respectively. This architecture enables the individual and synergistic effects of absorber coupling and interface engineering to be evaluated relative to the calibrated CdS-based reference device [42,43].

The proposed architecture has been systematically optimized with the aim of reducing interface recombination, strengthening the internal electric field, and expanding the effective absorption window. The results reveal that integrating $MAPbI_3$ as a secondary absorber at the $Sb_2Se_3$ interface significantly enhances charge-carrier separation and suppresses surface recombination due to the optimized energy alignment within the dual-absorber structure [26]. Furthermore, the addition of effectively mitigates the band mismatch between $MAPbI_3$ and ZnO and prevents charge accumulation at their interface [44–46]. Complementary analyses, including C–V, C–f, and Nyquist responses, indicate improved interfacial charge transport, reduced capacitance dispersion, and more stable frequency-dependent behavior [47–49]. These optical and electrical improvements collectively increase the power-conversion efficiency from 10.12% in the CdS based reference device to approximately 18.44% in the proposed structure, representing a substantial simulated performance enhancement compared with the calibrated $Sb_2Se_3$/CdS reference device.

In the subsequent sections of this study, a comprehensive set of optical and electrical analyses was performed to thoroughly evaluate the performance of the proposed device architecture. First, the simulated J–V characteristics were compared with those of the conventional $Sb_2Se_3$/CdS reference cell [14,46], clearly demonstrating substantial enhancements in Voc, $J_{sc}$, and FF achieved by introducing the $MAPbI_3$ layer. To elucidate the underlying mechanism of carrier extraction, the energy band diagram of the optimized structure was examined, highlighting the favorable band alignment and the improved separation of photogenerated carriers at the $Sb_2Se_3$/$MAPbI_3$ interface. The numerically generated Nyquist impedance responses were subsequently analyzed to estimate effective resistance and characteristic response parameters within the small-signal SCAPS-1D model. These quantities are model-derived predictions and should not be interpreted as

experimentally measured impedance parameters.

Furthermore, simulated capacitance–voltage (C–V) and capacitance–frequency (C–f) responses were calculated for two $MAPbI_3$ conductivity configurations to investigate their predicted depletion and trap-response behavior. These numerical analyses provide model-based insight into the electrostatic characteristics of the heterojunction but do not constitute experimental validation of interface quality. The optimized configuration showed superior frequency stability and lower interfacial charge accumulation. To optimize the optical absorption and charge-collection balance, a systematic thickness-dependent analysis of the $Sb_2Se_3$ absorber layer was carried out, revealing that a thickness of approximately 2.6 μm yields the highest power conversion efficiency (18.44%). In addition, the influence of $TiO_2$ buffer-layer thickness was investigated, demonstrating its critical role in suppressing interface traps and aligning the conduction-band offset with ZnO. Collectively, these simulations establish a coherent framework showing that the performance improvements originate from synergistic effects involving band-alignment engineering, recombination suppression, and geometrical-parameter optimization in the proposed dual-absorber heterostructure.

In addition to moisture and thermal degradation, photostability remains a major limitation for the practical deployment of perovskite solar cells. Continuous illumination may promote defect generation, iodide migration, interfacial reactions, and delamination between the perovskite and adjacent charge-transport layers. Recent work has therefore emphasized interface engineering strategies based on defect passivation, energy-level regulation, ion-migration barriers, and improved interfacial adhesion to reduce photodegradation [50,51]. Nevertheless, the effectiveness of such strategies is strongly dependent on the specific materials, interfaces, and operating conditions. Consequently, the inclusion of a $TiO_2$ interlayer in the present SCAPS-1D model should not be interpreted as experimental evidence of improved photostability.

## 2. Methodology and simulation details

The proposed $Sb_2Se_3/MAPbI_3/TiO_2/ZnO/Al:ZnO$ thin-film solar cell was numerically analyzed using SCAPS-1D version 3.3.11. SCAPS-1D self-consistently solves Poisson's equation together with the steady-state electron and hole continuity equations, while carrier recombination is described using the Shockley–Read–Hall formalism through the defined bulk and interface defect states. Unless otherwise specified, the simulations were performed at 300 K under the standard AM1.5G spectrum with an incident power density of 100 $mW{\cdot}cm^{-2}$. The final optimized device configuration used as the common baseline for all subsequent simulations was Al:ZnO (0.30 μm)/ ZnO (0.10 μm)/$TiO_2$ (0.02 μm)/$MAPbI_3$ (0.10 μm)/$Sb_2Se_3$ (2.60 μm)/$MoSe_2$ (1 μm)/Mo (1 μm). Unless a particular parameter was intentionally varied in a parametric analysis, all J-V, EQE, capacitance-frequency, temperature-dependent, and small-signal impedance calculations were performed using this single parameter set. All capacitance–voltage, capacitance–-frequency, impedance, and Nyquist results presented in this work were generated numerically using the small-signal AC analysis implemented in SCAPS-1D. No experimental impedance-spectroscopy or capacitance measurements were performed. Therefore, these results represent model-dependent predictions based on the specified material, defect, interface, contact, bias, and frequency parameters. Illumination was incident from the Al:ZnO front-contact side. The device consisted sequentially of Al:ZnO, ZnO, $TiO_2$, $MAPbI_3$, and $Sb_2Se_3$, followed by the rear Mo contact. The voltage, current, and spatial-coordinate conventions were kept identical for the reference and proposed devices to ensure a direct comparison.

The external contacts were defined through carrier-selective boundary conditions rather than by assuming ideal recombination-free contacts. The front Al:ZnO contact was assigned a work function of 4.30 eV, with electron and hole surface-recombination velocities of $10^7$ and $10^2$ $cm.s^{-1}$, respectively. The rear Mo contact was assigned a work function of 5.10 eV, with electron and hole surface-recombination velocities $10^7$ and $10^2$ $cm.s^{-1}$, respectively. External series resistance and shunt conductance were disabled in the final simulations ($R_s$= 0 $\Omega cm^2$ and $G_{sh}$=0 $S.cm^{-2}$, corresponding to $R_{sh}\rightarrow\infty$ ). A possible $MoSe_2$ interfacial layer was not explicitly modeled; therefore, its chemical formation and time-dependent evolution remain beyond the scope of the present simulation.

Although a thin $MoSe_2$ interfacial layer may form in experimentally fabricated devices, it was not explicitly included as a separate layer in the present simulation. Instead, its effect is implicitly incorporated through the interface recombination parameters defined at the $Sb_2Se_3$/back-contact interface.

Material parameters, including layer thickness, bandgap, electron affinity, relative permittivity, effective density of states, carrier mobilities, doping concentrations, and defect densities, were adopted from experimentally reported literature and are summarized in Table 1 with corresponding references.

The thickness values of each layer were selected based on a combination of experimentally reported ranges and systematic parametric optimization. Initial thicknesses were adopted from literature reports on similar - and perovskite-based thin-film solar cells to ensure physically realistic modeling conditions. Subsequently, parametric studies were carried out to evaluate the influence of key layer thicknesses on device performance. In particular, the thickness of the $Sb_2Se_3$ absorber and the $TiO_2$ buffer layer were systematically varied to determine the optimal trade-off between optical absorption, carrier transport, and recombination losses. The thicknesses of other layers ($MAPbI_3$, ZnO, and Al:ZnO) were selected within experimentally validated ranges and kept fixed to maintain stable transport conditions and avoid additional resistive limitations. The adopted thickness ranges are consistent with previously reported experimental and simulation studies [7,15,25,37].

Wavelength-dependent absorption coefficients for each layer were imported into SCAPS-1D to ensure realistic photogeneration and accurate calculation.

Bulk recombination was described using single neutral Shockley–Read–Hall defect levels positioned near the middle of the corresponding bandgap. Electron and hole thermal velocities were set to $10^7$ $cm.s^{-1}$, and electron and hole capture cross-sections were fixed at $10^{-15}$ $cm^2$ . The effective bulk-defect densities were $10^{15}$ $cm^{-3}$ for Al: ZnO, ZnO, $TiO_2$, and CdS $10^{14}$ $cm^{-3}$, for $MAPbI_3$ $3\times10^{14}$ $cm^{-3}$, and for $Sb_2Se_3$ 1 $\times$ $10^{14}$ $cm^{-3}$. Interface defects were also represented by single neutral levels with electron and hole capture cross-sections of $10^{-15}$ $cm^2$ . The interface-state densities used at the Al:ZnO/ZnO, ZnO/$TiO_2$, $TiO_2$/$MAPbI_3$, and $MAPbI_3$ / $Sb_2Se_3$ interfaces were $1\times10^{11}$, $5\times10^{11}$, $1\times10^{12}$, and $5\times10^{11}$ $cm^{-2}$, respectively. Direct radiative and Auger recombination were disabled, and recombination was therefore governed by the defined bulk and interface SRH states.

The thickness of the $MAPbI_3$ layer was fixed at 100 nm throughout the simulations. Due to its high absorption coefficient in the visible region ($\sim10^5$ $cm^{-1}$), $MAPbI_3$ can efficiently absorb photons even at relatively small thicknesses. Increasing its thickness beyond this value provides only marginal optical gain while potentially introducing additional recombination and transport losses. Therefore, the optimization process was primarily focused on the $Sb_2Se_3$ absorber layer, which plays the dominant role in determining the overall device performance. Preliminary simulations further confirmed that variations in $MAPbI_3$ thickness have a relatively minor impact on the overall device efficiency compared to the absorber thickness.

Following calibration and validation of the reference device, parametric simulations were performed to evaluate the effects of $Sb_2Se_3$ absorber thickness, $TiO_2$ interlayer thickness, $MAPbI_3$ conductivity type, and operating temperature. The electrical response was subsequently examined using J-V, EQE, capacitance-frequency, and small-signal impedance calculations. The calibration procedure and its agreement with the experimental reference data are presented in the following section before the proposed device is introduced.

**Table 1**
Physical and electronic parameters used in the SCAPS-1D simulation.

| Layer | Thickness (μm) | Bandgap (Eg, eV) | Electron affinity (χ, eV) | Relative permittivity ($\varepsilon_r$) | Nc ($cm^{-3}$) | Nv ($cm^{-3}$) | μn ($cm^2$/V·s) | μp ($cm^2$/V·s) | $N_A$($cm^{-3}$) | $N_D$($cm^{-3}$) | Conductivity type |
|---|---|---|---|---|---|---|---|---|---|---|---|
| Al:ZnO (TCO) | 0.3 | 3.30 | 4.30 | 9.0 | $2.2\times10^{18}$ | $1.8\times10^{19}$ | 50 | 25 | 0 | $1\times10^{18}$ | $n^+$-type |
| ZnO (ETL) | 0.1 | 3.30 | 4.30 | 9.0 | $2.2\times10^{18}$ | $1.8\times10^{19}$ | 100 | 25 | 0 | $1\times10^{17}$ | n-type |
| $TiO_2$ (Buffer) | 0.02 | 3.20 | 4.00 | 31.0 | $2.2\times10^{18}$ | $1.8\times10^{19}$ | 10 | 1 | 0 | $1\times10^{17}$ | n-type |
| $MAPbI_3$ (Secondary-Absorber) | 0.1 | 1.55 | 3.90 | 25.0 | $2.2\times10^{18}$ | $1.8\times10^{19}$ | 20 | 10 | 0 | $1\times10^{16}$ | n-type |
| $Sb_2Se_3$ (Primary-Absorber) | 2.6 | 1.20 | 4.00 | 15.0 | $2.2\times10^{18}$ | $1.8\times10^{19}$ | 15 | 5 | $1\times10^{16}$ | 0 | p-type |

The present model assumes laterally uniform, one-dimensional semiconductor layers with spatially averaged material and defect properties. Effects associated with local grain orientation, grain-boundary anisotropy, pinholes, lateral current non-uniformity, ion migration in $MAPbI_3$, chemical reactions between adjacent layers, contact degradation, and time-dependent environmental ageing are not explicitly included. In addition, the majority-carrier-selective contact conditions represent an idealized approximation. The calculated photovoltaic parameters should therefore be interpreted as physically constrained numerical projections for the specified parameter set rather than as guaranteed experimental device performance.

It should be emphasized that the present SCAPS-1D model evaluates steady-state electronic and optical behavior and does not constitute a lifetime or degradation model. The simulations do not explicitly include ion migration, moisture or oxygen ingress, phase decomposition, elemental interdiffusion, contact corrosion, residual mechanical stress, delamination, ultraviolet-induced degradation, or irreversible thermally activated reactions. Accordingly, the temperature-dependent calculations quantify the intrinsic electrical sensitivity of the specified parameter set but cannot predict long-term operational stability or device lifetime under outdoor conditions.

## 3. Calibration and validation

As mentioned in the previous section, a novel thin-film solar cell architecture based on $Sb_2Se_3$/$MAPbI_3$/$TiO_2$/*ZnO/Al:ZnO* has been designed and numerically simulated in this paper. As depicted in Fig. 1 (a), the $Sb_2Se_3$ layer serves as the primary absorber, while the $MAPbI_3$ layer acts as a secondary absorber, forming a heterojunction interface with a staggered band alignment that enables efficient carrier separation and reduced recombination losses. The wide-bandgap $TiO_2$ layer (~3.2 eV) is introduced as an electron transport and buffer layer between $MAPbI_3$ and ZnO to minimize band misalignment and suppress interface-related losses. Subsequently, the *ZnO* and *Al:ZnO* layers function as electron transport and transparent conductive oxide (TCO) layers, facilitating electron extraction toward the external electrode. This energy-engineered multilayer configuration allows for broader spectral absorption, stronger built-in field-assisted charge separation, and significant improvement in photovoltaic performance parameters such as $J_{sc}$, $V_{oc}$, and overall efficiency.

The physical and electronic parameters of each layer, including thickness, energy bandgap ($E_g$), work function, carrier mobility, and doping type, are summarized in Table 1. To ensure realistic modeling, interface recombination effects at the layer interfaces and experimentally derived absorption coefficients for each material were also incorporated into the simulation. For validation purposes, the numerical model was first calibrated using a reference device structure reported in [14]. The simulation parameters, such as carrier lifetimes, defect densities, and interface properties, were adjusted to reproduce the reported performance metrics of the reference device. All simulations were carried out under standard AM1.5G illumination (100 $mW{\cdot}cm^{-2}$). Wavelength-dependent absorption coefficients for $Sb_2Se_3$, ZnO, and Al:ZnO were imported into SCAPS-1D based on experimentally reported optical data, ensuring realistic photogeneration and $J_{sc}$ calculation.

Fig. 1(a), presents the external quantum efficiency (EQE) spectra of the solar cell, comparing our simulation results with the experimental data reported in reference [14]. The simulation curve closely follows the experimental trend across the full spectral range of 300–1100 nm, demonstrating high accuracy in modeling optical absorption and carrier collection processes. The EQE reaches a maximum of approximately 85–90% around the visible region, indicating efficient photogeneration. Additionally, the integrated short-circuit current density ($J_{sc}$), calculated from both experimental and simulated EQE data, shows very good agreement, confirming the reliability of the simulation model for predicting device photocurrent response. Fig. 1(b), compares the measured and simulated J–V characteristics under standard AM 1.5 illumination. The results demonstrate a strong overlap between experimental data points and the simulated curve, particularly in the near-short-circuit and near-open-circuit regions. The simulated short-circuit current density and open-circuit voltage values align well with experimental measurements, validating the accuracy of the electrical modeling and recombination mechanisms incorporated into the device structure. The minor deviation near open-circuit voltage can be attributed to interface recombination and series-resistance effects not fully captured by the idealized simulation environment. Fig. 1(c), illustrates the dependence of on incident light intensity over a range spanning nearly two orders of magnitude. Both simulation and experimental data exhibit a linear relationship in the log-log scale, characterized by a slope close to unity, indicating that the photocurrent is predominantly generation-limited. The close match between the two curves highlights the robustness of the simulation model in capturing carrier transport dynamics under varying illumination conditions. This consistency further confirms that the device operates efficiently across a broad spectrum of solar irradiance levels.

## 4. Proposed device structure and band alignment

Fig. 2(a) illustrates the schematic configuration of the proposed dual-absorber thin-film solar cell, designed to enhance optical absorption and charge collection by integrating two complementary absorber layers. The bottom absorber layer is $Sb_2Se_3$, which serves as the primary material due to its highly suitable bandgap, strong absorption coefficient, and excellent carrier transport properties. Above it, the $MAPbI_3$ perovskite layer is introduced as a secondary absorber, enabling efficient absorption in the visible region and facilitating the formation of a p–n heterojunction with enhanced built-in electric field. This dual-absorber strategy broadens the spectral response range, improves photon-to-electron conversion efficiency, and reduces recombination losses by promoting efficient separation of photogenerated carriers across the heterointerface.

On top of the absorber stack, a $TiO_2$ layer is employed as a buffer and electron transport layer (ETL), providing efficient extraction of electrons

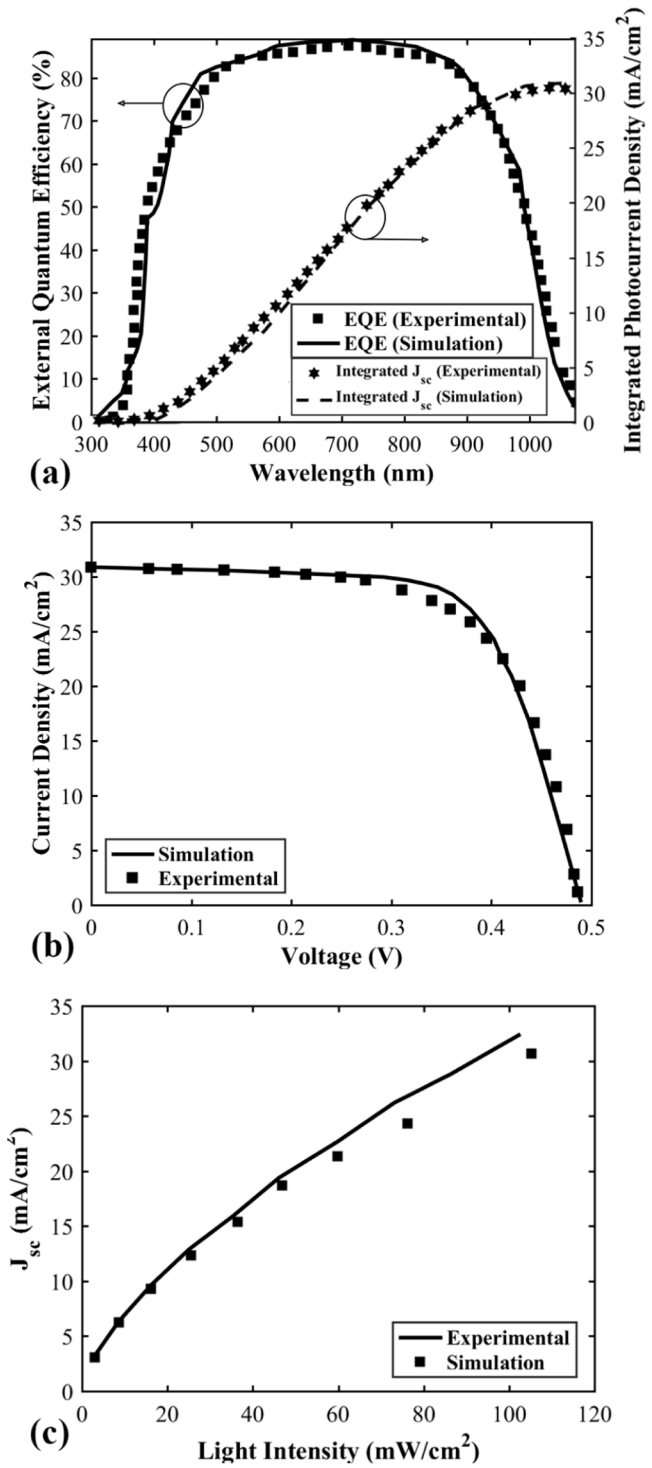


**Fig. 1.** Comprehensive comparison between experimental data [14] and simulation results for $Sb_2Se_3$ cells, showcasing: (a) EQE (b) J-V (c) Light-intensity-dependent short-circuit current ($J_{sc}$) curves.

from $MAPbI_3$ while simultaneously suppressing interfacial recombination.

The ZnO layer positioned above the $TiO_2$ acts as an electron transport layer (ETL), providing a low-resistance pathway for electron extraction due to its high electron mobility and wide bandgap. From a band-alignment perspective, ZnO forms a favorable conduction band cascade with $TiO_2$, which facilitates directional electron transport toward the front contact while minimizing energy barriers. This alignment reduces carrier accumulation at the interface and suppresses recombination losses, thereby contributing to improved charge collection efficiency and fill factor.

Finally, the Al-doped ZnO (Al:ZnO) layer functions as a transparent conductive oxide (TCO), allowing incident light to enter the device while providing a low-resistance pathway for electron transport toward the metal contact. This multilayer architecture is carefully engineered to achieve balanced carrier extraction, minimal resistive losses, and high photovoltaic efficiency, demonstrating the potential of hybrid perovskite/$Sb_2Se_3$ configurations for next-generation solar cell technologies.

From an experimental perspective, the feasibility of forming an $Sb_2Se_3/MAPbI_3$ interface is supported by a previously fabricated Mo/$Sb_2Se_3/MAPbI_3/C_{60}$/GZO/Ag planar heterojunction device [26]. This result demonstrates that $MAPbI_3$ can be sequentially deposited in contact with $Sb_2Se_3$ under appropriately controlled processing conditions. However, it does not establish the chemical stability or fabrication compatibility of the complete $Sb_2Se_3/MAPbI_3/TiO_2$/ZnO/Al:ZnO stack proposed in the present work. The SCAPS-1D model assumes laterally uniform layers and an abrupt, chemically stable $Sb_2Se_3/MAPbI_3$ interface and does not explicitly account for interfacial reactions, elemental interdiffusion, ion migration, surface roughness, pinhole formation, residual stress, or time-dependent phase evolution. Therefore, experimental analyses such as X-ray photoelectron spectroscopy, X-ray diffraction or GIWAXS, cross-sectional electron microscopy with elemental mapping, and time-resolved photoluminescence would be required to verify the composition, morphology, and electronic quality of the fabricated interface [15].

In the proposed design (See Fig. 2(a)), $Sb_2Se_3$ acts as a stable low-bandgap absorber, while $MAPbI_3$ serves as a higher-bandgap absorber to enable stepwise photon harvesting in a heterojunction configuration. $TiO_2$ functions as an electron transport/buffer layer (ETL), providing strong adhesion between $MAPbI_3$ and ZnO and mitigating interfacial trap formation. Subsequently, ZnO and Al:ZnO layers act as electron extraction and transparent conducting layers, respectively, contributing to reduced series resistance and enhanced electron transport. This design aims to balance efficient light absorption with effective charge extraction, ultimately improving the power conversion efficiency (η), fill factor (FF), and short-circuit current density ($J_{sc}$).

Fig. 2(b), illustrates the equilibrium energy band diagram of the proposed Cell heterostructure under zero-bias conditions. The diagram clearly demonstrates the relative alignment of the conduction band minimum (CBM) and valence band maximum (VBM) across the multilayer device, providing insight into the charge transport and recombination mechanisms. The pronounced spike observed in the $TiO_2$ region originates from the positive conduction band offset (CBO) at the $MAPbI_3/TiO_2$ heterointerface, which arises from the difference in electron affinity between $Sb_2Se_3$ and $MAPbI_3$. This upward step in the conduction band edge forms a moderate selective barrier that suppresses hole back-diffusion toward the electron transport layers, thereby reducing interfacial recombination. Importantly, the spike height remains sufficiently small to allow efficient electron transport via thermionic emission and tunneling mechanisms, and therefore does not introduce significant transport losses.

At the $Sb_2Se_3/MAPbI_3$ interface, a staggered (type-II) band alignment is formed, where the conduction band edge of $MAPbI_3$ lies slightly below that of $Sb_2Se_3$, while its valence band edge is deeper. This configuration promotes efficient spatial separation of photogenerated carriers: electrons are preferentially transferred from $Sb_2Se_3$ into $MAPbI_3$, whereas holes remain confined within the $Sb_2Se_3$ absorber. Such spatial decoupling significantly suppresses interfacial electron-hole recombination and contributes to an enhanced quasi-Fermi level splitting, which directly impacts the open-circuit voltage.

The apparent spike observed in the conduction band profile within the $TiO_2$ region originates from the positive conduction band offset (CBO) at the $MAPbI_3/TiO_2$ heterointerface. This offset arises from the difference in electron affinity between $MAPbI_3$ and $TiO_2$, leading to an

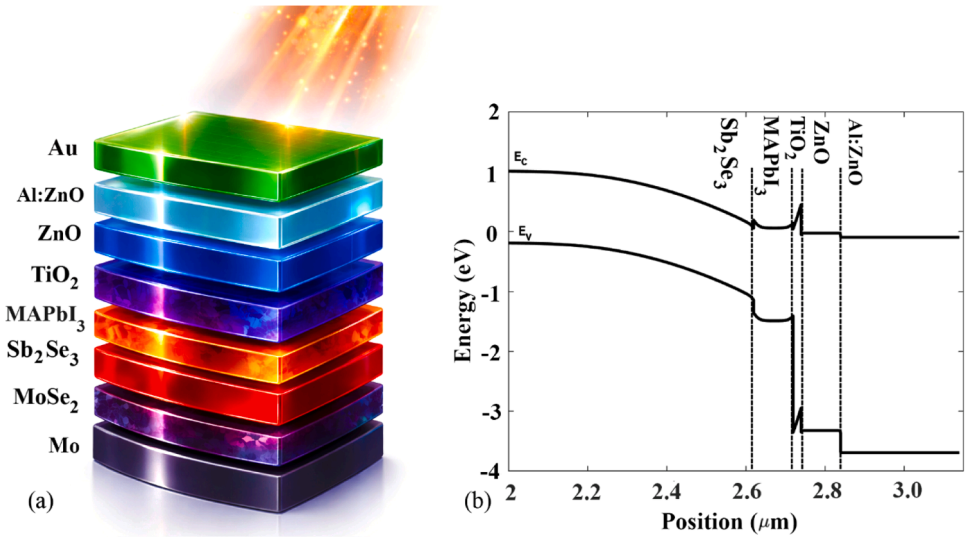


**Fig. 2.** (a), Schematic illustration of the proposed Mo/$MoSe_2$/$Sb_2Se_3$/$MAPbI_3$/$TiO_2$/ZnO/Al:ZnO/Au thin-film solar cell structure. The $Sb_2Se_3$ layer acts as the primary absorber, $MAPbI_3$ as the secondary absorber, $TiO_2$ as an electron-transport and buffer layer, and ZnO/Al:ZnO serve as the electron-transport and transparent conductive layers, respectively. Arrows indicate the direction of electron and hole transport under illumination. (b), Simulated equilibrium energy band diagram of the $Sb_2Se_3$/$MAPbI_3$/$TiO_2$/ZnO/Al:ZnO device showing type-II alignment and favorable carrier transport pathways.

upward step in the conduction band edge when electrons transition from $MAPbI_3$ into the $TiO_2$ layer.

Physically, this moderate conduction band spike plays a beneficial selective-contact role rather than acting as a transport barrier. The spike suppresses the back-diffusion of minority carriers (holes) from $MAPbI_3$ toward the electron transport layers, thereby reducing interfacial recombination losses. At the same time, the spike height remains sufficiently small to allow efficient electron transport via thermionic emission and tunneling mechanisms, preventing any significant degradation of current density or fill factor. It should be noted that the magnitude of this positive CBO (~0.1 eV) lies within the commonly reported tolerance window for electron-selective contacts, where moderate variations in the offset do not introduce transport barriers but effectively suppress interfacial recombination.

Furthermore, the $TiO_2$ layer smooths the abrupt band discontinuity between $MAPbI_3$ and ZnO, resulting in a more gradual band bending across the electron transport region. This reduction in band abruptness mitigates charge accumulation at the $MAPbI_3$/ZnO interface, which is commonly associated with increased recombination and resistive losses. As a result, the dominant electrical improvement introduced by $TiO_2$ is reflected primarily in the enhancement of the fill factor rather than in a pronounced increase in short-circuit current or open-circuit voltage.

Therefore, the observed spike is a direct consequence of deliberate band alignment engineering and represents an optimized compromise between carrier selectivity and transport efficiency. Such controlled conduction band spikes are widely recognized as an effective strategy for suppressing interfacial recombination while maintaining efficient charge extraction in high-performance thin-film solar cells.

The ZnO and Al:ZnO layers provide a favorable downward band alignment toward the front contact, ensuring efficient electron transport and collection. Meanwhile, the built-in electric field across the absorber region is strengthened due to the combined effect of band bending and reduced recombination, contributing to the overall enhancement in device performance.

Overall, the energy band diagram confirms that the performance improvement in the proposed device originates primarily from optimized band alignment and recombination suppression enabled by the $MAPbI_3$/$TiO_2$ stack, rather than from increased optical absorption alone [14].

## 5. Simulation results and discussions

Table 1, summarizes the physical and electronic parameters employed in the SCAPS simulation to model the multilayer solar cell structure. The device consists of a transparent conductive oxide (TCO) layer of Al-doped ZnO (Al:ZnO), followed by ZnO as the electron transport layer (ETL), a $TiO_2$ buffer layer, a $MAPbI_3$ perovskite layer, and an $Sb_2Se_3$ layer, all integrated to form the optimized dual-absorber configuration. Each layer's thickness, bandgap ($E_g$), electron affinity ($\chi$), and relative permittivity ($\varepsilon_r$) were selected based on experimentally reported material properties to accurately emulate optical absorption, carrier generation, and electric-field distribution within the cell. The bandgap values range from 3.3 eV for the wide-bandgap Al:ZnO and ZnO layers to 1.2 eV for $Sb_2Se_3$, ensuring broad spectral absorption while maintaining efficient charge separation through favorable band alignment [28].

In addition to physical thickness and optical constants, the electronic parameters including effective density of states in the conduction and valence bands ($N_c$ and $N_v$), carrier mobilities ($\mu_n$ and $\mu_p$), doping type, and concentration are also listed in Table 1. These values directly influence charge transport, recombination dynamics, and overall device performance. For example, high electron mobility in ZnO (100 $cm^2/V{\cdot}s$) supports efficient electron extraction, while moderate hole mobility in $Sb_2Se_3$ (5 $cm^2/V{\cdot}s$) reflects typical characteristics of this material system. The doping concentrations range from $1 \times 10^{18}$ $cm^{-3}$ in Al:ZnO/$1 \times 10^{16}$ $cm^{-3}$ in the absorber layers, representing realistic levels used to optimize built-in potential and reduce recombination losses. Together, these parameters provide a comprehensive foundation for accurate numerical simulation and enable meaningful comparison between simulated electrical characteristics and experimental reports [14].

The Interface parameters, including defect densities ($N_t$), recombination velocities, and conduction/valence band offsets (CBO/VBO), are defined according to literature-reported values and optimized to achieve stable junction characteristics [39]. A small positive CBO (0.1 eV) at the $TiO_2$/$MAPbI_3$ and $MAPbI_3$/$Sb_2Se_3$ interfaces facilitate electron transport while preventing hole backflow, confirming the band alignment responsible for efficient charge separation Table 2.

Fig. 3 (a), illustrates the J–V characteristics of the proposed and reference thin-film solar cells under standard AM1.5 illumination.

The optimized proposed device exhibits $J_{sc}$=34.05 $mA.cm^{-2}$, $V_{oc}$=0.77V, FF=70.34%, and a power conversion efficiency of 18.44%.

**Table 2**
Interface parameters and band offsets used in the SCAPS-1D simulation.

| Interface | Interface defect density ($N_{ti}$, $cm^{-2}$) | Recombination velocity (cm/s) | $\Delta E_c = E_{c,right} - E_{c,left}$ | $\Delta E_v = E_{v,right} - E_{v,left}$ | Description / Notes |
|---|---|---|---|---|---|
| Al:ZnO / ZnO | $1 \times 10^{11}$ | $1 \times 10^{2}$ | 0.00 | 0.00 | Ohmic contact, negligible band offset |
| ZnO / $TiO_2$ | $5 \times 10^{11}$ | $5 \times 10^{3}$ | -0.30 | -0.40 | Favorable conduction band energy; promotes electron extraction |
| $TiO_2$ /$MAPbI_3$ | $1 \times 10^{12}$ | $1 \times 10^{4}$ | +0.10 | -1.75 | Small positive CBO (spike), acts as hole-blocking barrier |
| $MAPbI_3$ / $Sb_2Se_3$ | $5 \times 10^{11}$ | $1 \times 10^{5}$ | +0.10 | -0.25 | Alignment enabling carrier separation |
| $Sb_2Se_3$ / Back Contact (Mo) | $1 \times 10^{12}$ | $1 \times 10^{6}$ | — | — | Ohmic back contact; ensures hole extraction |

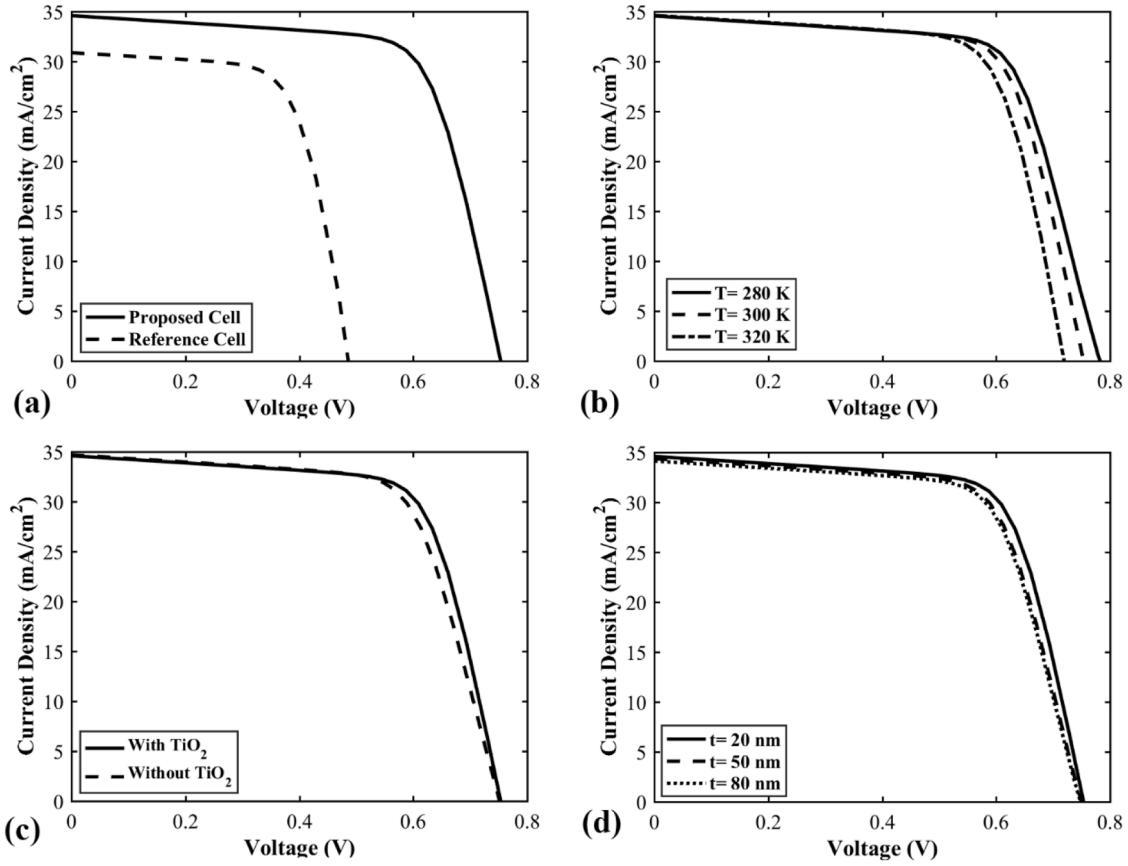


**Fig. 3.** (a). Simulated current–voltage (J–V) characteristics of the reference cell and the proposed device under AM1.5G illumination (1000 W/m$^2$). (b). Simulated J–V characteristics of the proposed solar cell at different operating temperatures (280 K, 300 K, and 320 K) under standard AM1.5G illumination (1000 W). (c). J–V curves of the proposed structure with and without the buffer layer, demonstrating improved current and voltage due to enhanced carrier transport and reduced recombination. (d). Effect of thickness on the J–V characteristics; the optimal thickness (20 nm) ensures efficient charge extraction with minimal series resistance.

In comparison, the calibrated $Sb_2Se_3$/CdS reference device exhibits $J_{sc}$=30.86 mA.cm$^{-2}$, $V_{oc}$=0.48 V, FF=67.19%, and an efficiency of 10.12%, indicating a significant enhancement in carrier separation and extraction efficiency. The improvement in Jsc originates from the dual-absorber configuration of $Sb_2Se_3$ and $MAPbI_3$, which enables broader spectral absorption. Specifically, $MAPbI_3$ efficiently absorbs photons in the visible region (400-750 nm), while $Sb_2Se_3$ extends the absorption into the near-infrared region (750-1100 nm). The incorporation of the $TiO_2$ buffer layer between $MAPbI_3$ and ZnO effectively suppresses interfacial trap states and minimizes electron-hole recombination at the heterointerface. The increase in $V_{oc}$ is attributed to the stronger built-in electric field at the $Sb_2Se_3$/$MAPbI_3$ interface and the formation of a band alignment, which facilitates directional carrier transport and reduces surface recombination [8]. More specifically, the type-II band alignment at the $Sb_2Se_3$/$MAPbI_3$ interface promotes spatial separation of photogenerated carriers, where electrons are driven toward $MAPbI_3$ while holes remain in $Sb_2Se_3$. This separation reduces interfacial recombination and enhances quasi-Fermi level splitting, leading to an increase in open-circuit voltage. In addition, the improved band alignment facilitates directional carrier transport and reduces carrier accumulation at the interface, which contributes to enhanced short-circuit current density. Furthermore, the presence of a small positive conduction band offset (~0.1 eV) at the $MAPbI_3$/$TiO_2$ interface provides electron selectivity by blocking hole backflow while allowing efficient electron transport. This selective-contact behavior reduces recombination losses and improves the diode quality, resulting in an enhanced fill factor. Therefore, the overall improvement in device performance can be directly attributed to the optimized band alignment and its impact on carrier separation, transport, and recombination dynamics. Furthermore, the presence of high-mobility electron transport layers ($TiO_2$ and

ZnO) lowers the series resistance, thereby improving the fill factor (FF ≈ 70%). Overall, the proposed device achieves a power conversion efficiency of approximately 18.44%, representing a considerable improvement over the reference cell [14]. These findings confirm that replacing the CdS buffer with $MAPbI_3$ and introducing a $TiO_2$ interlayer is an effective strategy to enhance the optoelectronic performance of $Sb_2Se_3$ based thin-film solar cells.

The J-V characteristics of the proposed solar cell at different temperatures (280 K, 300 K, and 320 K) under AM1.5 illumination is depicted in Fig. 3(b). As the temperature increases from 280 K to 320 K, the open-circuit voltage ($V_{oc}$) decreases noticeably, while the short-circuit current density ($J_{sc}$) exhibits only a minor variation. This trend is consistent with semiconductor physics, as higher temperatures lead to increased intrinsic carrier concentration, enhanced recombination rates, and a reduction in the quasi-Fermi level splitting, thereby lowering $V_{oc}$. In contrast, a slight rise in Jsc at higher temperatures can be attributed to the reduced series resistance and marginally improved carrier mobility [18]. However, the $V_{oc}$ loss dominates which results in a decrease in overall device efficiency. According to simulation results, the efficiency (η) decreases from 18.44% at 300 K to 17.4% at 320 K, whereas a slightly higher efficiency of 18.7% is achieved at 280 K. Overall, the results confirm that the proposed structure exhibits limited electrical sensitivity over the investigated temperature range, with only minor Voc degradation over the studied temperature range. The stability of Jsc and FF across temperatures further validates the robust interfacial quality and efficient charge transport pathways within the hybrid heterostructure. It should be noted that the temperature range investigated in this study (280-320 K) corresponds to typical operating conditions of thin-film solar cells and is primarily intended to assess the intrinsic thermal sensitivity of the electrical performance parameters within a steady-state transport framework. Thermal degradation mechanisms reported for $Sb_2Se_3$ based structures at elevated temperatures, such as phase instability, ion migration, and chemical decomposition, involve kinetic and chemical processes that are not explicitly captured by SCAPS-1D simulations and therefore lie beyond the scope of the present work. Fig. 3(c) presents the J-V characteristics of the proposed device with and without the $TiO_2$ layer. The results indicate that the incorporation of $TiO_2$ does not result in a pronounced change in the open-circuit voltage ($V_{oc}$), while the variation in short-circuit current density ($J_{sc}$) also remains limited. Instead, the dominant improvement induced by the $TiO_2$ interlayer is observed in the fill factor (FF) [20]. This enhancement in FF indicates that $TiO_2$ primarily functions as an effective electron-selective buffer between $MAPbI_3$ and ZnO, facilitating electron extraction while suppressing interfacial recombination and hole leakage. The improved band alignment at the $MAPbI_3/TiO_2/ZnO$ interfaces mitigate transport barriers and leads to a more ideal diode--like J-V response. Consequently, the increase in FF emerges as the main contributor to the overall improvement in power conversion efficiency, whereas changes in $J_{sc}$ and $V_{oc}$ play a secondary role.

Eventually, as shown in Fig. 3(d), the influence of thickness on the J–V performance of the proposed device was systematically investigated for thicknesses of 20 nm, 50 nm, and 80 nm in order to elucidate the trade-off between carrier selectivity and resistive transport losses. The simulated J–V curves reveal that the 20 nm layer yields the most

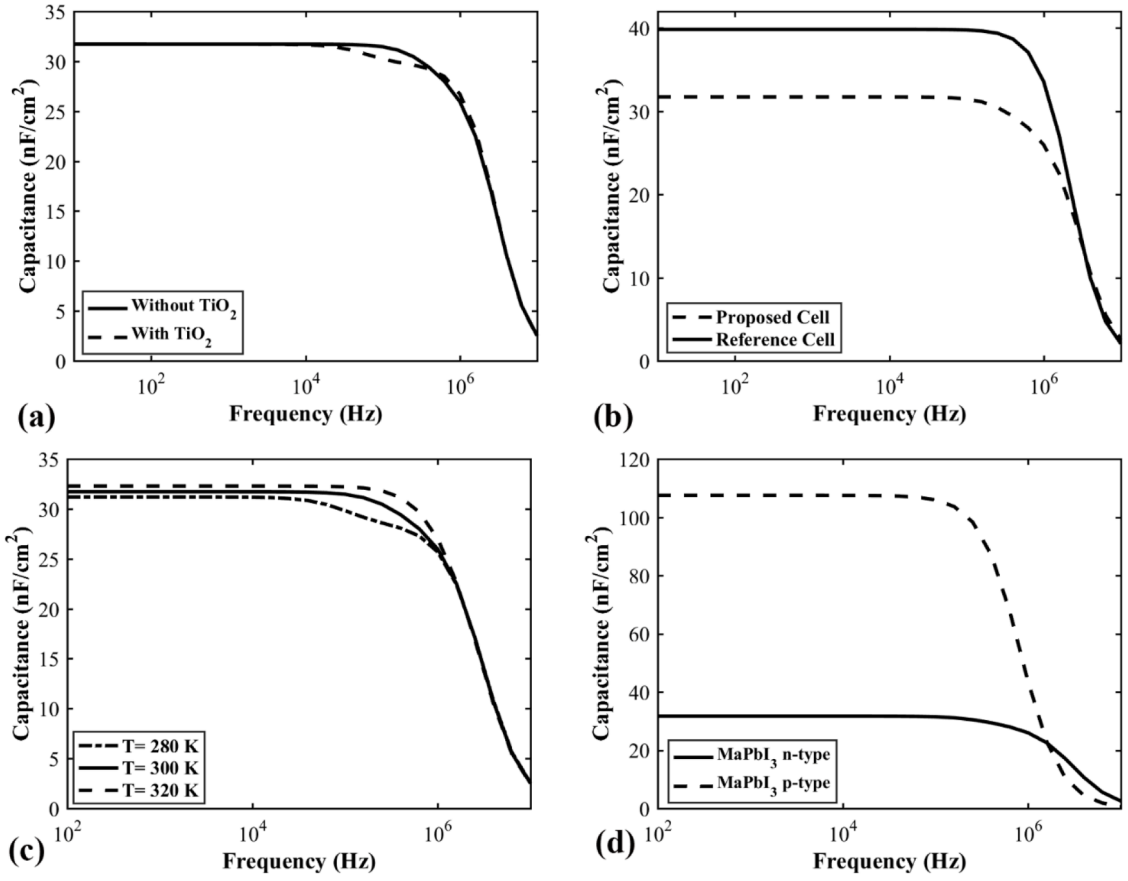


**Fig. 4.** (a). Capacitance-frequency (C-f) response of the proposed device with and without the $TiO_2$ buffer. The $TiO_2$ containing structure exhibits slightly lower low-frequency capacitance and improved frequency stability, indicating reduced interfacial trap-mediated charge accumulation. (b). Comparison of C-f curves for the reference and proposed devices. The proposed cell exhibits slightly reduced low-frequency capacitance, consistent with an extended depletion width and diminished interfacial trap capacitance. (c). Temperature dependence of the C-f response for the proposed device (280 K, 300 K, 320 K). A modest increase in low-frequency capacitance with temperature reflects enhanced thermal activation of trap states and increased intrinsic carrier concentrations at elevated temperatures. (d). Simulated capacitance–frequency (C-f) characteristics of the proposed solar cell for different conductivity types of the $MAPbI_3$ layer.

favorable overall photovoltaic response, with higher, and FF compared with the thicker configurations, while the curves corresponding to 50 nm and 80 nm are nearly coincident and consistently inferior across all three parameters. In particular, the fill factor (FF) obtained with the 20 nm layer is clearly higher than that of the 50 nm and 80 nm cases, indicating that increasing the buffer-layer thickness beyond 20 nm introduces additional series resistance and reduces carrier-transport efficiency without providing any compensating gain in photocurrent or voltage. For excessively thin layers (< 20 nm), insufficient hole-blocking leads to enhanced interfacial recombination at the interface. Consequently, an optimal thickness of approximately 20 nm represents the best compromise between carrier selectivity and transport resistance, yielding the highest overall device efficiency. It should be emphasized that $TiO_2$ is a wide-bandgap oxide (Eg ≈ 3.2 eV) and therefore exhibits negligible absorption in the visible and near-infrared spectral range. Accordingly, the observed performance variations with $TiO_2$ thickness primarily originate from electrical effects, such as carrier selectivity and transport resistance, rather than parasitic optical losses.

Consistent with the simulated J-V behavior, the numerically calculated capacitance-frequency response of the proposed device with and without the $TiO_2$ buffer layer is presented in Fig. 4(a). Both configurations exhibit an approximately constant capacitance at low frequencies (below 105 Hz), followed by a roll-off at higher frequencies. The inclusion of $TiO_2$ leads to a slight reduction in low-frequency capacitance and improved frequency stability, which can be attributed to the suppression of interfacial trap states and reduced charge accumulation at the $MAPbI_3$/ZnO interface. Acting as an electron-selective buffer, $TiO_2$ smooths the band alignment and mitigates slow trap responses, resulting in faster capacitive transitions [52]. Furthermore, Fig. 4(b) compares the C–f characteristics of the conventional reference device and the proposed structure. At low frequencies, the proposed device exhibits a lower capacitance, indicating an expanded effective depletion width and reduced interfacial trap density. This improvement originates from the favorable band alignment at the heterojunction, which promotes efficient carrier separation and suppresses recombination [17]. At higher frequencies, both devices converge toward the same geometric capacitance, reflecting intrinsic dielectric contributions. The reduced capacitance dispersion and enhanced frequency stability of the proposed device are consistent with its improved charge extraction and stronger built-in electric field compared to the *CdS*-based architecture [7].

The simulated temperature-dependent C–f responses of the proposed device at 280, 300, and 320 K are presented in Fig. 4(c). By increasing temperature, a slight rise in the low-frequency capacitance and a minor shift of the roll-off frequency toward higher values are observed. This can be attributed to the enhanced thermal activation of shallow trap states and the faster charge discharge dynamics of interfacial traps at elevated temperatures [53]. Nevertheless, the overall similarity of the simulated curves indicates that the small-signal capacitance response is only moderately sensitive to temperature within the investigated 280–320 K range. This result reflects the electrical response of the predefined interface-defect model and does not demonstrate that $TiO_2$ prevents chemical or structural degradation under prolonged thermal stress. Verification of such a stabilizing effect would require temperature-dependent experimental impedance measurements and accelerated ageing of devices fabricated with and without the $TiO_2$ interlayer.

In Fig. 4(d), the capacitance-frequency (C-f) behavior of the proposed structure was analyzed for two different conductivity types of the $MAPbI_3$ layer. As illustrated in Fig. 4(d), the switch between these two conduction modes has a significant influence on the capacitive behavior of the heterostructure.

In heterojunction solar cells, the total capacitance is primarily determined by the depletion region of the p-n junction and can be expressed as [5]:

$$C = \frac{\varepsilon A}{W} \tag{1}$$

where, $\varepsilon$ is the effective dielectric constant, A is the device area, and W represents the depletion width.

The depletion width depends on the effective doping concentration and the applied bias as follows [31]:

$$W = \sqrt{\frac{2\varepsilon(V_{bi} - V)}{qN_{eff}}} \tag{2}$$

where, $q$ is the electronic charge, $V_{(\beta i)}$ the built-in potential, and $N_{eff}$ the effective doping density.

Consequently, the inverse square of capacitance varies linearly with bias according to:

$$\frac{1}{C^2} = \frac{2(V_{bi} - V)}{q\varepsilon N_{eff}} \tag{3}$$

This classical C-V relation forms the basis for interpreting frequency dependent capacitance, where the presence of interface traps and finite carrier response time modulate the C-f profile.

### 5.1. Configuration with wider depletion region

In this structure, the main junction forms between the $Sb_2Se_3$ absorber layer and the $MAPbI_3$ layer, generating a strong built-in electric field at their interface. Due to the relatively low doping density in one layer and higher carrier concentration in the other, the depletion width becomes wider, leading to a lower overall capacitance according to the above relation. The C-f curve shows an almost constant capacitance over the entire frequency range with only a minor variation at low frequencies, indicating fast carrier response and negligible charge accumulation at the interfaces. This behavior corresponds to an ideal junction capacitance and can be modeled as [9]:

$$C_{total} \approx \left(\frac{1}{C_{Sb_2Se_3}} + \frac{1}{C_{MAPbI_3}}\right)^{-1} \tag{4}$$

where $C_i = \frac{\varepsilon_i A}{W_i}$ for each layer. For this configuration, the depletion width $W_{MAPbI_3}$ increases, resulting in a reduced total capacitance and a more stable frequency response.

### 5.2. Configuration with Confined Depletion Region

In contrast, when the dominant junction forms between the $MAPbI_3$ layer and the $TiO_2$ layer, the $Sb_2Se_3/MAPbI_3$ interface (composed of two layers with similar characteristics) does not contribute to a significant depletion region. Consequently, the depletion width becomes confined to the thin $MAPbI_3/TiO_2$ interface, leading to a higher overall capacitance:

$$C_{p-type} > C_{n-type} \tag{5}$$

Moreover, a visible increase in capacitance at low frequencies is observed, which arises from interfacial charge accumulation and the slow response of trap states at the $MAPbI_3/TiO_2$ boundary. This pseudo-capacitive behavior can be described by a parallel RC model [9]:

$$C(\omega) = \frac{C_0}{\sqrt{1 + (\omega\tau)^2}} \tag{6}$$

where, is the angular frequency and τ is the trap response time. At low frequencies ( ≪ 1), the traps can charge and discharge, leading to a large capacitance, whereas at high frequencies ( ≫ 1) the capacitance saturates at .

Fig. 5 (a), presents the Nyquist plots of the proposed and reference

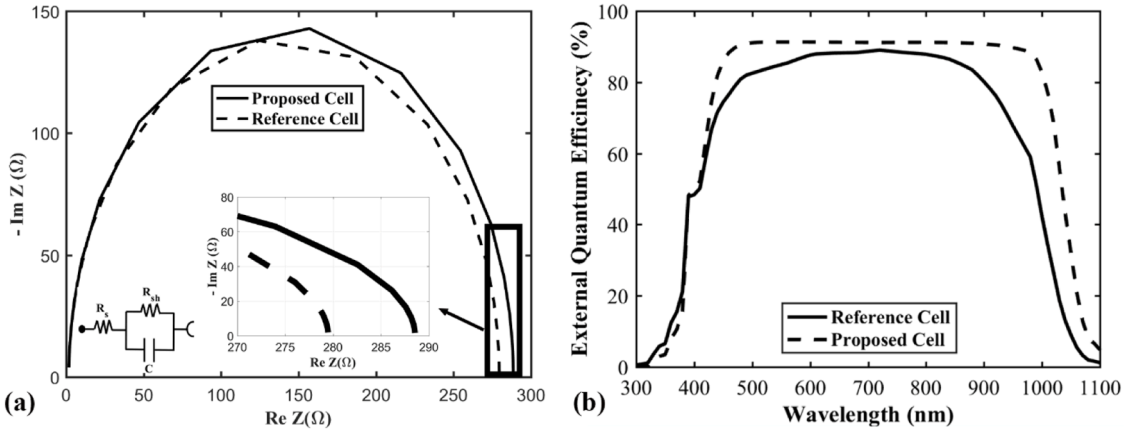


**Fig. 5.** (a). Nyquist plots of the reference and proposed solar cells under illumination. The proposed device exhibits a slightly modified semicircular response, indicating a modest change in interfacial resistance and charge-transport dynamics. Quantitative resistance values were extracted by fitting the spectra to the equivalent circuit shown in the inset. (b). External quantum efficiency (EQE) spectra of the reference and proposed cells. The proposed dual-absorber device exhibits enhanced EQE across the visible range (due to $MAPbI_3$) and extended response into the near-IR (due to $Sb_2Se_3$), resulting in a higher integrated $J_{sc}$.

solar cell structures, illustrating the relationship between the real (Re Z) and imaginary (Im Z) components of the impedance. Nyquist analysis provides valuable insight into the resistive and capacitive processes governing charge transport and recombination within the device.

Both devices exhibit a characteristic semicircular response in the intermediate frequency range, which is commonly associated with the charge transfer resistance ($R_{ct}$) at the heterointerfaces, followed by a high-frequency response related to bulk transport and dielectric relaxation. The overall impedance behavior suggests that interfacial processes play a dominant role in determining the electrical performance of both structures.

Compared to the reference cell, the proposed device exhibits a Nyquist response with a similar semicircle radius, accompanied by a slight reduction in the proposed structure. Although this difference is not pronounced, it suggests a marginal decrease in charge-transfer resistance and a modest improvement in interfacial charge transport. The impedance response therefore indicates a subtle enhancement in carrier extraction efficiency, rather than a fundamental change in the

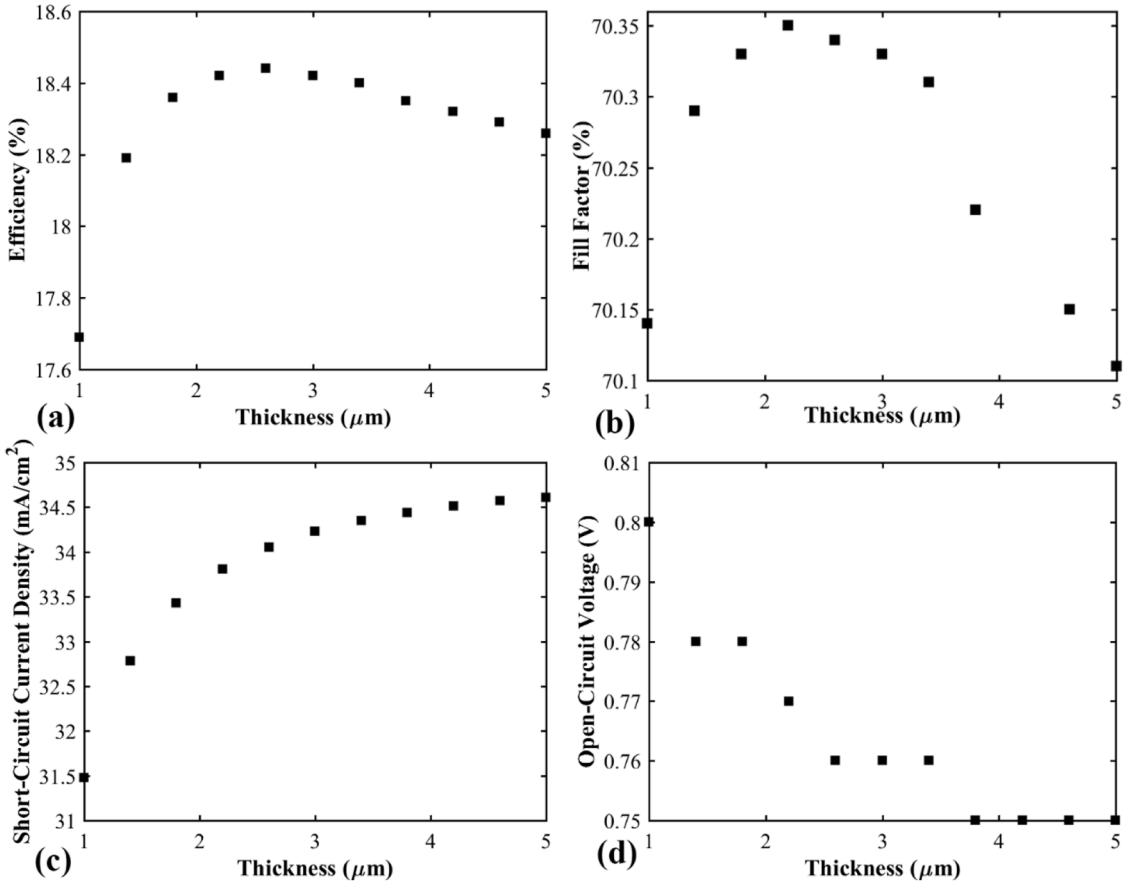


**Fig. 6.** Variation of (a) power conversion efficiency (η), (b) fill factor (FF), (c) short-circuit current density ($J_{sc}$), and (d) open-circuit voltage ($V_{oc}$) as a function of the $Sb_2Se_3$ absorber thickness in the proposed $Sb_2Se_3/MAPbI_3/TiO_2/ZnO/Al:ZnO$ structure.

dominant transport mechanism.

The observed impedance behavior can be attributed to the improved band alignment and reduced density of interfacial defect states at the $Sb_2Se_3$/$MAPbI_3$ interface. A lower defect density mitigates non-radiative recombination pathways and facilitates smoother carrier transport across the junction, thereby reducing resistive losses.

Overall, the simulated Nyquist response suggests a modest change in the effective interfacial resistance of the proposed device within the adopted SCAPS-1D model. Since no experimental impedance measurement or independent equivalent-circuit fitting was performed, this result should be interpreted as a qualitative numerical indication rather than experimental confirmation of interface quality or recombination dynamics. leading to slightly lower internal resistances and enhanced charge transport characteristics. These electrical improvements are consistent with the observed enhancement in device performance, primarily manifested through improved charge collection and fill factor, rather than pronounced changes in the open-circuit voltage or short-circuit current density.

The external quantum efficiency (EQE) spectra of the reference and proposed solar cells are presented in Fig. 5(b). The proposed device exhibits an enhanced EQE in the 400-800 nm range, which is mainly attributed to efficient photon absorption in the $MAPbI_3$ layer. In addition, a measurable photo response extends up to ~1100 nm, corresponding to absorption in the $Sb_2Se_3$ absorber. Although $Sb_2Se_3$ is present in both devices, the significantly higher EQE of the proposed cell in the long-wavelength region (800-1100 nm) cannot be explained by absorption alone. In this spectral range, photocarriers are generated deeper inside the $Sb_2Se_3$ layer and their collection become strongly limited by interfacial recombination and electric-field strength. In the reference $Sb_2Se_3$/CdS device, less favorable band alignment and higher interfacial recombination reduce the collection efficiency of these long-wavelength carriers. In contrast, the improved band alignment and reduced recombination at the $Sb_2Se_3$/$MAPbI_3$ interface enable more efficient extraction of photocarriers, resulting in a higher EQE despite similar optical absorption.

The EQE-integrated current density is approximately 34.6 $mA.cm^{-2}$, which differs by about 1.6% from the J–V-derived value of 34.05 $mA.cm^{-2}$. This small deviation is attributed to spectral discretization and numerical integration, in close agreement with the J-V results, while the reference cell yields about 31 $mA.cm^{-2}$. These results confirm that the enhanced EQE originates primarily from improved carrier collection efficiency rather than increased optical absorption [22].

The device power-conversion efficiency (η) as a function of $Sb_2Se_3$ absorber thickness is depicted in Fig. 6(a). A maximum efficiency of 18.44% is obtained at an $Sb_2Se_3$ thickness of 2.6 μm, resulting from a trade-off between optical gain and electronic loss: increasing thickness enhances photon harvesting and thus, but also increases carrier transport distance and volumetric recombination. For thicknesses below the optimum, optical under-absorption limits performance; for thicknesses above the optimum, bulk/interfacial recombination reduces and FF, lowering . The optimum therefore corresponds to the thickness at which enhanced absorption and deleterious recombination are balanced. This conclusion is consistent with the concurrent trends in $J_{sc}$, $V_{oc}$ and FF shown in panels Fig. 6(c) and 6(d).

Fig. 6 (b), presents the fill factor as a function of thickness. The fill factor increases slightly up to the optimum region and subsequently decreases at higher thicknesses. The initial enhancement results from improved carrier collection and reduced effective series losses, whereas the reduction at larger thicknesses is caused by increased series resistance, enhanced recombination, and distortion of the I–V characteristics. These trends highlight the strong dependence of the electronic quality of the device on absorber thickness.

In Fig. 6 (c), a monotonic increase in the short-circuit current density with increasing thickness is observed. A thicker absorber enhances photon harvesting, particularly near the band-edge region, which leads to higher . However, an increase in does not necessarily guarantee improved overall efficiency, as excessive thickness may limit carrier collection and intensify recombination. Hence, must be interpreted in conjunction with the corresponding voltage-related parameters.

A gradual decrease in the open-circuit voltage with increasing absorber thickness is demonstrated in Fig. 6 (d). The reduction in is attributed to an increase in the dark saturation current and higher recombination rates in thicker layers. Additionally, longer carrier transport paths and enhanced internal voltage losses further contribute to this decline. This behavior confirms that electronic limitations dominate at larger thicknesses, counteracting the optical benefits gained from increased absorption.

**Table 3**
Comparison of the simulated photovoltaic parameters of the proposed device with selected experimentally reported $Sb_2Se_3$-based solar cells.

| Research Case | $V_{oc}$ (V) | $J_{sc}$ ($mA/cm^2$) | FF (%) | η (%) | Reference |
|---|---|---|---|---|---|
| Experimental | 0.57 | 10.23 | 55.34 | 3.21 | [54] |
| Experimental | 0.39 | 26.25 | 57.83 | 5.94 | [55] |
| Experimental | 0.42 | 25.49 | 59.34 | 6.52 | [56] |
| Experimental | 0.488 | 30.879 | 67.18 | 10.12 | [14] |
| Simulation | 0.77 | 34.05 | 70.34 | 18.44 | This work |

## 6. Comparison of experimental data with proposed solar cell

Table 3, provides a comprehensive comparison of the photovoltaic performance of $Sb_2Se_3$ based solar cells reported in earlier experimental studies and the proposed device. As observed, The substantial improvements in $J_{sc}$, $V_{oc}$, and FF obtained in the proposed device arise from three main mechanisms: (1) the incorporation of $MAPbI_3$ as a wide-bandgap secondary absorber, which enhances photon harvesting and carrier generation, (2) the formation of a band alignment at the $Sb_2Se_3$/$MAPbI_3$ interface that promotes efficient charge separation and suppresses interface recombination, and (3) the inclusion of a $TiO_2$ buffer layer that adjusts the $MAPbI_3$/ZnO band offset, reduces interface traps, and prevents carrier leakage. Together, these modifications significantly improve charge extraction and reduce resistive and recombination losses.

The efficiency enhancement from 10.12% in the reference cell [14] to 18.44% in the proposed device results from simultaneous improvement of three key parameters: (1) the increase in $J_{sc}$ from 25-30 $mA/cm^2$ in experimental reports to ~34 $mA/cm^2$, (2) the rise in $V_{oc}$ from 0.39-0.57 V to 0.77 V, and (3) the improvement of FF to ~70%, indicating significantly reduced recombination and series resistance losses. This coordinated enhancement confirms the simultaneous optimization of both optical absorption and charge transport in the proposed architecture.

Overall, the comparative analysis demonstrates that precise interface engineering and replacing CdS with an efficient secondary absorber ($MAPbI_3$), combined with a $TiO_2$ buffer layer, can effectively overcome the intrinsic limitations of conventional $Sb_2Se_3$/CdS devices. This study indicates that an optimized $Sb_2Se_3$-based dual-absorber architecture may achieve a simulated cell-level efficiency exceeding 18%. However, translation of this projected performance to a practical and reliable module requires experimental fabrication, scale-up, encapsulation, and long-term environmental validation.

## 7. Practical feasibility, fabrication challenges, and operational reliability

Although the numerical results demonstrate the potential electrical advantages of the proposed architecture, the exact proposed device has not yet been experimentally fabricated. Therefore, the simulated performance should be regarded as a design target rather than an experimentally demonstrated device efficiency. The previously reported fabrication of a Mo/$Sb_2Se_3$/$MAPbI_3$/$C_{60}$/GZO/Ag heterojunction

supports the basic feasibility of sequentially forming an $Sb_2Se_3$/$MAPbI_3$ absorber interface. Nevertheless, the addition of the $TiO_2$/ZnO/Al:ZnO stack introduces further processing and interface-compatibility requirements that must be experimentally evaluated.

A potential fabrication sequence would involve deposition of the Mo rear contact on a thermally stable substrate, followed by growth of the absorber using a controlled vapor-phase process. The thin $MAPbI_3$ layer could subsequently be deposited by a low-temperature solution or vapor-based route. The most critical processing step would then be the formation of $TiO_2$, ZnO, and Al:ZnO above the temperature- and chemically sensitive $MAPbI_3$ layer. These oxide layers would require low-temperature and low-damage deposition conditions. Possible approaches include low-temperature atomic-layer deposition or other conformal soft-deposition methods, followed by carefully controlled deposition of ZnO and Al:ZnO. However, plasma exposure, energetic particle bombardment, reactive oxygen species, solvents, and thermal annealing may alter the $MAPbI_3$ composition or introduce interface defects. The $TiO_2$ layer must also be continuous and pinhole-free while remaining sufficiently thin to avoid excessive transport resistance.

Additional fabrication challenges include obtaining uniform coverage of the 100-nm $MAPbI_3$ layer over the relatively thick $Sb_2Se_3$ absorber, controlling the surface roughness and crystallographic orientation of $Sb_2Se_3$, preventing interfacial voids and delamination, and maintaining reproducible band alignment over a large area. Direct contact between $MAPbI_3$ and ZnO has previously been associated with accelerated interfacial and thermal degradation. The proposed $TiO_2$ layer may reduce direct $MAPbI_3$/ZnO interaction and improve carrier selectivity; however, the present simulation only predicts its electronic effect and cannot demonstrate chemical passivation or enhanced lifetime. These functions must be verified through structural characterization and comparative ageing experiments performed on devices with and without $TiO_2$.

The field studies on module ageing further demonstrate that module ageing cannot be evaluated solely from initial J–V parameters. Changes in temperature coefficients, internal resistance, visual appearance, delamination, corrosion, hot-spot formation, and other optical and non-optical failures can be correlated with long-term performance degradation under outdoor conditions. Although those studies concern established PV module technologies rather than the specific $Sb_2Se_3$/$MAPbI_3$ chemistry considered here, they provide an important module-level reliability framework. Future experimental work should therefore combine material-specific stability analysis with standardized module qualification and long-term outdoor monitoring before the commercial viability of the proposed architecture can be assessed.

## 8. Future perspective toward practical PV module implementation

The photovoltaic parameters reported in this work were obtained for an idealized one-dimensional cell and do not directly represent the performance of a large-area module. Translation of the proposed architecture into a practical thin-film PV module would require scalable deposition of a substrate/Mo/$MoSe_2$/$Sb_2Se_3$/$MAPbI_3$/$TiO_2$/ZnO/Al:ZnO stack, followed by electrical integration of individual cell stripes. A possible approach would be monolithic series interconnection using P1, P2, and P3 patterning steps for the back contact, semiconductor stack, and transparent conductive electrode, respectively. However, the compatibility of laser or mechanical scribing with $MAPbI_3$ and the adjacent interfaces would need to be established because local heating, debris formation, and edge damage may generate shunts or accelerate degradation.

Scale-up would also introduce performance losses that are not included in the present SCAPS-1D model. These include the sheet resistance of the Al:ZnO transparent electrode, contact and interconnection resistance, inactive scribe areas, lateral current transport, cell-to-cell mismatch, nonuniform illumination, and thickness or defect-density variations across the module area. In particular, reproducible deposition of a compact and pinhole-free 100-nm $MAPbI_3$ layer over large-area, followed by conformal low-damage formation of $TiO_2$, ZnO, and Al:ZnO, represents a significant fabrication challenge. Consequently, module efficiency would be expected to remain below the simulated active-area cell efficiency until these geometrical and resistive losses are minimized.

Encapsulation would be essential because the $MAPbI_3$ layer is susceptible to moisture, oxygen, elevated temperature, and prolonged illumination. A potential module package could employ a glass–glass architecture incorporating a low-temperature moisture- and oxygen-barrier encapsulant together with hermetic edge sealing. The encapsulant should provide high optical transmission, ultraviolet stability, strong adhesion, low water-vapor and oxygen permeability, and mechanical compliance to accommodate thermal-expansion mismatch between the glass, metal, oxide, and perovskite layers. Because $MAPbI_3$ contains Pb, the package should additionally incorporate Pb-retention or Pb-sequestration functionality to reduce environmental release if the module is mechanically damaged.Low-temperature encapsulation approaches have shown improved damp-heat and thermal-cycling resistance and substantial suppression of Pb leakage in perovskite photovoltaic devices and modules; however, their chemical and mechanical compatibility with the present $Sb_2Se_3$/$MAPbI_3$ architecture must be independently verified [57,58].

The temperature-dependent results presented in this study describe the steady-state electrical response of the defined SCAPS parameter set over 280–320 K and should not be interpreted as proof of long-term module-level thermal stability. In a practical module, repeated daily and seasonal temperature changes can modify contact resistance, interfacial adhesion, encapsulant properties, and defect activity. Temperature coefficients should therefore be determined experimentally under stabilized operating conditions and monitored during ageing. Recent field analysis has shown that variations in the temperature coefficients of maximum power, open-circuit voltage, and short-circuit current can provide complementary information about optical and non-optical PV-module failures, including delamination, corrosion, and abnormal thermal behavior [59].

Environmental durability should be evaluated through damp-heat, thermal-cycling, humidity-freeze, ultraviolet-exposure, mechanical-load, hail-impact, insulation, reverse-bias, and stabilized maximum-power-point tests, followed by long-term outdoor monitoring under representative climatic conditions. Field investigations of differently aged PV modules have demonstrated that initial electrical performance alone is insufficient for assessing reliability and that visual, electrical, thermal, and insulation inspections are required to identify degradation and permanent failure modes. Although those investigations were performed on established module technologies rather than the specific $Sb_2Se_3$/$MAPbI_3$ structure proposed here, they provide a relevant module-reliability framework for future validation.

Therefore, assessment of commercial viability will require more than verification of the simulated cell efficiency. It will depend on large-area fabrication yield, module efficiency after geometric and resistive losses, encapsulation and interconnection costs, operational lifetime, Pb containment, recyclability, and compliance with relevant module qualification requirements. The present architecture should accordingly be regarded as a cell-level numerical design framework. Pilot-scale module fabrication, accelerated ageing, outdoor exposure, and techno-economic and environmental assessments are required before its practical or commercial viability can be established.

## 9. Conclusion

A Cd-free $Sb_2Se_3$/$MAPbI_3$/$TiO_2$/ZnO/Al:ZnO thin-film solar cell was numerically investigated using a calibrated SCAPS-1D model. Through interface and band-alignment engineering, the proposed dual-absorber architecture achieves a simulated power conversion efficiency of

18.44%, significantly higher than the 10.12% efficiency of the conventional $Sb_2Se_3$/CdS reference device. The performance enhancement originates from the type-II band alignment at the $Sb_2Se_3$/$MAPbI_3$ interface and the electron-selective role of the $TiO_2$ interlayer, which collectively improve charge separation, suppress recombination losses, and enhance $V_{oc}$, $J_{sc}$, and fill factor. In addition, replacing CdS improves environmental compatibility, although the presence of Pb in $MAPbI_3$ means that the device should be considered a partially green solution rather than fully non-toxic. The specific contribution of the present study is therefore not the individual selection of $Sb_2Se_3$, $MAPbI_3$, or $TiO_2$, which have previously been investigated in different photovoltaic configurations. Rather, it is the experimentally calibrated, $Sb_2Se_3$-centered redesign of a conventional CdS-based device and the controlled evaluation of the separate and combined roles of the $MAPbI_3$ secondary absorber and the $TiO_2$ interface-engineering layer. From a broader perspective, the proposed dual-absorber strategy provides a pathway toward next-generation photovoltaic technologies by combining complementary absorbers to extend spectral utilization and by employing interface engineering to control recombination and carrier selectivity. Such an approach is consistent with emerging trends in tandem and hybrid solar cells, where multi-absorber configurations are used to overcome the efficiency limitations of single-junction devices. It is important to emphasize that the objective of this work is to provide a physically grounded design framework for dual-absorber $Sb_2Se_3$-based solar cells, rather than to achieve the highest reported efficiency. Despite the promising results, practical implementation challenges remain, including interface quality control, $MAPbI_3$ stability, and fabrication complexity. Therefore, further experimental studies are required to validate the proposed design and address these limitations.

## Ethical approval statement

The authors confirm that the submitted paper has not been submitted to any other journal and that this version is original and has not been published elsewhere. Additionally, all listed authors affirm the integrity of the study, data, information, and analyses, ensuring that no manipulations have been made. Furthermore, we confirm that no other individuals meet the authorship criteria for this paper beyond those listed as authors.

## CRediT authorship contribution statement

**Danial Keighobadi:** Writing – original draft, Software, Investigation, Data curation, Conceptualization. **Ali Asghar Orouji:** Writing – review & editing, Validation, Software. **Mehdi Mousavi-Kamazani:** Validation, Supervision, Data curation, Conceptualization. **Mohammad Danaie:** Writing – review & editing, Supervision, Project administration, Formal analysis, Conceptualization.

## Declaration of competing interest

The authors declare that they have no known competing financial interests or personal relationships that could have appeared to influence the work reported in this paper.

## Funding

The authors declare that no funds, grants, or financial support were received for the preparation of this manuscript.

## Data availability

Data will be made available on request.

## References

[1] N. Asim, et al., A review on the role of materials science in solar cells, Renew. Sustain. Energy Rev. 16 (8) (2012) 5834–5847.
[2] A.S. Al-Ezzi, M.N.M. Ansari, Photovoltaic solar cells: a review, Appl. Syst. Innov. 5 (4) (2022) 67.
[3] P. Choubey, A. Oudhia, R. Dewangan, A review: solar cell current scenario and future trends, Recent Res. Sci. Technol. 4 (8) (2012).
[4] Z.-S. Wang, et al., Significant influence of TiO2 photoelectrode morphology on the energy conversion efficiency of N719 dye-sensitized solar cell, Coord. Chem. Rev. 248 (13-14) (2004) 1381–1389.
[5] T.D. Lee, A.U. Ebong, A review of thin film solar cell technologies and challenges, Renew. Sustain. Energy Rev. 70 (2017) 1286–1297.
[6] T. Kirchartz, U. Rau, What makes a good solar cell? Adv. Energy Mater. 8 (28) (2018) 1703385.
[7] C. Chen, K. Li, J. Tang, Ten Years of $Sb_2Se_3$ thin film solar cells, Sol. RRL 6 (7) (2022) 2200094.
[8] N. Kant, P. Singh, Review of next generation photovoltaic solar cell technology and comparative materialistic development, Mater. Today: Proc. 56 (2022) 3460–3470.
[9] F. Mujtahid, et al., Review effect of various types of dyes and structures in supporting performance of dye-sensitized solar cell TiO2-based nanocomposites, Int. J. Energy Res. 46 (2) (2022) 726–742.
[10] A.S. Bati, et al., Next-generation applications for integrated perovskite solar cells, Commun. Mater. 4 (1) (2023) 2.
[11] S. Chen, et al., (Zn, Ti) O electron transport layer enables the highest conversion efficiency in Cd-Free Sb2Se3 photocathodes for stable solar hydrogen production, Adv. Mater. (2026) e18202.
[12] P. Luo, et al., Electron transport layer engineering induced carrier dynamics optimization for efficient Cd-free Sb2Se3 thin-film solar cells, Small 20 (4) (2024) 2306516.
[13] S. Chen, et al., Simultaneous Band Alignment Modulation and Carrier Dynamics Optimization Enable Highest Efficiency in Cd-Free Sb2Se3 Solar Cells, Adv. Funct. Mater. 34 (40) (2024) 2403934.
[14] Z. Duan, et al., Sb2Se3 thin-film solar cells exceeding 10% power conversion efficiency enabled by injection vapor deposition technology, Adv. Mater. 34 (30) (2022) 2202969.
[15] A. Geravand, S. Sharbati, M. Danaie, Optimize parameters of new fabricated n-CdTe/p-CdTe solar cell, in: 2017 Iranian Conference on Electrical Engineering (ICEE), IEEE, 2017.
[16] M. Danaie, A. Geravand, Design of low-cross-talk metal–insulator–metal plasmonic waveguide intersections based on proposed cross-shaped resonators, J. Nanophotonics 12 (4) (2018), 046009–046009.
[17] X. Wang, et al., Interfacial engineering for high efficiency solution processed Sb2Se3 solar cells, Sol. Energy Mater. Sol. Cells 189 (2019) 5–10.
[18] I. Gharibshahian, A.A. Orouji, S. Sharbati, Towards high efficiency Cd-Free Sb2Se3 solar cells by the band alignment optimization, Sol. Energy Mater. Sol. Cells 212 (2020) 110581.
[19] I. Gharibshahian, A.A. Orouji, S. Sharbati, Alternative buffer layers in Sb2Se3 thin-film solar cells to reduce open-circuit voltage offset, Sol. Energy 202 (2020) 294–303.
[20] Z.-Q. Li, M. Ni, X.-D. Feng, Simulation of the Sb2Se3 solar cell with a hole transport layer, Mater. Res. Express 7 (1) (2020) 016416.
[21] M. Al-Hattab, et al., Numerical simulation of a new heterostructure CIGS/GaSe solar cell system using SCAPS-1D software, Sol. Energy 227 (2021) 13–22.
[22] U. Daraz, et al., Fabrication, characterization, and photocatalytic performance of ternary cadmium chalcogenides CdIn2S4 and Cd7. 23Zn2. 77S10-ZnS thin films, Main Group Met. Chem. 44 (1) (2021) 39–50.
[23] I. Gharibshahian, A.A. Orouji, S. Sharbati, Efficient Sb2 (S, Se) 3/Zn (O, S) solar cells with high open-circuit voltage by controlling sulfur content in the absorber-buffer layers, Sol. Energy 227 (2021) 606–615.
[24] X. Jin, et al., Controllable solution-phase epitaxial growth of Q1D Sb2 (S, Se) 3/CdS heterojunction solar cell with 9.2% efficiency, Adv. Mater. 33 (44) (2021) 2104346.
[25] K. Maurya, V. Singh, Sb2Se3 versus Sb2S3 solar cell: a numerical simulation, Sol. Energy 228 (2021) 540–549.
[26] G. Wu, et al., Study of antimony selenide hole-transport material for Mo/Sb2Se3/MAPbI3/C60/GZO/Ag heterojunction planar solar cells, Surf. Coat. Technol. 405 (2021) 126550.
[27] T. Wu, et al., The main progress of perovskite solar cells in 2020–2021, Nano-Micro Lett. 13 (1) (2021) 152.
[28] A. Ait Abdelkadir, et al., Numerical simulation and optimization of n-Al-ZnO/n-CdS/p-CZTSe/p-NiO (HTL)/Mo solar cell system using SCAPS-1D, Results Opt. 8 (2022) 100257.
[29] M.F. Rahman, et al., A qualitative design and optimization of CIGS-based solar cells with Sn2S3 back surface field: a plan for achieving 21.83% efficiency, Heliyon 9 (12) (2023).
[30] S. Rawat, R. Gupta, S. Gohri, Performance assessment of CIGS solar cell with different CIGS grading profile, Mater. Today: Proc. (2023).
[31] Y. Gong, et al., Elemental de-mixing-induced epitaxial kesterite/CdS interface enabling 13%-efficiency kesterite solar cells, Nat. Energy 7 (10) (2022) 966–977.
[32] M. Jost, et al., Perovskite/CIGS tandem solar cells: from certified 24.2% toward 30% and beyond, ACS energy lett. 7 (4) (2022) 1298–1307.
[33] R. Lu, et al., Highly efficient (200) oriented MAPbI3 perovskite solar cells, Chem. Eng. J. 433 (2022) 133845.
[34] P. Roy, et al., Perovskite solar cells: a review of the recent advances, Coatings 12 (8) (2022) 1089.

[35] F. Shahnooshi, A.A. Orouji, A. Abbasi, Enhanced performance of Graphene/AlGaAs/GaAs heterostructure Schottky solar cell using AlGaAs drainage, J. Mater. Sci.: Mater. Electron. 33 (7) (2022) 4617–4627.
[36] Y. Singh, et al., Sb2Se3 heterostructure solar cells: Techniques to improve efficiency, Sol. Energy 249 (2023) 174–182.
[37] J.J. Yoo, S.S. Shin, J. Seo, Toward efficient perovskite solar cells: progress, strategies, and perspectives, ACS Energy Lett. 7 (6) (2022) 2084–2091.
[38] J. Zhu, et al., Interfacial charge and surface defect regulation for high-efficiency CdIn2S4-based photoanodes, Appl. Surf. Sci. 601 (2022) 154188.
[39] T. Chargui, et al., Experimental and numerical study of the CIGS/CdS heterojunction solar cell, Opt. Mater. 140 (2023) 113849.
[40] S. Khatoon, et al., Simulation study of CsPbIxBr1-x and MAPbI3 heterojunction solar cell using SCAPS-1D, Sol. Energy 254 (2023) 137–157.
[41] M.A.H. Pappu, et al., Design of n-CdS/p-CuInTe2/p+-MoS2 thin film solar cell with a power conversion efficiency of 34.32%, Opt. Contin. 2 (4) (2023) 942–955.
[42] X. Ma, et al., Facile fabrication of CdIn2S4/TiO2 heterojunction for enhanced solar light efficient CO2 reduction, Front. Chem. Sci. Eng. 18 (9) (2024) 105.
[43] M.A. Hamza, G.F. Metha, C.J. Shearer, Recent advances and future directions of CdIn 2 S 4-based photocatalysts: properties, synthesis, and modifications for energy and environmental applications, J. Mater. Chem. A 13 (27) (2025) 21292–21351.
[44] G. Yadav, M. Ahmaruzzaman, CdIn2S4-based advanced composite materials: Structure, properties, and applications in environment and energy–A concise review, Inorg. Nano-Met. Chem. 55 (2) (2025) 122–136.
[45] Z. Kadiroglu, The Role of Cation Deficiency and Impurities in the Formation of Photosensitivity Centers in CdIn2S4 Compound, Phys. Solid State 67 (8) (2025) 684–687.
[46] D. Keighobadi, M. Mousavi-Kamazani, M. Danaie, Enhancing Sb2Se3 thin-film solar cell efficiency via CuGaSe2 dual-absorber integration, Sci. Rep. (2026).
[47] S.M. Sivasankar, C.d.O. Amorim, A.F.d. Cunha, Progress in thin-film photovoltaics: A review of key strategies to enhance the efficiency of CIGS, CdTe, and CZTSSe solar cells, J. Compos. Sci. 9 (3) (2025) 143.
[48] F. Shahnooshi, A.A. Orouji, Efficiency improvement of graphene/AlGaAs/GaAs Schottky junction solar cells by minimizing optical losses through front and rear surface texturing, Sci. Rep. 15 (1) (2025) 21520.
[49] D. Keighobadi, M. Mousavi-Kamazani, M. Danaie, Optimizing Sb2Se3 solar cells with CdIn2S4 buffer for high-efficiency and stability: a comprehensive analysis, Mater. Des. (2026) 115912.
[50] K. Sang, et al., Improving photostability of perovskite solar cells by interface engineering for emerging applications, Innov. Inform. 1 (1) (2025), 100004–1.
[51] K. Sang, et al., Ligand-Induced in Situ Epitaxial Growth of PbI2 Nanosheets/MAPbI3 Heterojunction Realizes High-Performance HTM-Free Carbon-Based MAPbI3 Solar Cells, Small Methods 8 (9) (2024) 2301531.
[52] Q. Fatima, et al., A critical review on advancement and challenges in using TiO2 as electron transport layer for perovskite solar cell, Mater. Today Sustain. 27 (2024) 100857.
[53] M. Li, et al., Improving the efficiency and stability of MAPbI3 perovskite solar cells by dipeptide molecules, Small 20 (25) (2024) 2311400.
[54] H. Deng, et al., Efficient and stable TiO2/Sb2S3 planar solar cells from absorber crystallization and Se-atmosphere annealing, Mater. Today Energy 3 (2017) 15–23.
[55] L. Wang, et al., Stable 6%-efficient Sb2Se3 solar cells with a ZnO buffer layer, Nat. Energy 2 (4) (2017) 1–9.
[56] C. Chen, et al., 6.5% certified efficiency Sb2Se3 solar cells using PbS colloidal quantum dot film as hole-transporting layer, ACS Energy Lett. 2 (9) (2017) 2125–2132.
[57] N. Belhaouas, et al., Comprehensive analysis and insights into the relationship between temperature coefficients, PV failures, and investigating their correlation with other PV parameters, Sol. Energy 301 (2025) 113891.
[58] N. Belhaouas, et al., Failures and performance of different aged PV modules operated under northern Algerian climate conditions: Analysis, assessment, and recommended solutions, Eng. Fail. Anal. 163 (2024) 108504.
[59] D. Keighobadi, et al., Enhanced Performance of $Sb_2Se_3$-Based Solar Cells with Fe doped CuGa (S, Te) 2 as a Secondary Absorber, Mater. Today Commun. (2026) 115301.